Biophysical Reports

Cooled SPAD array detector for low light-dose fluorescence laser scanning microscopy

Eli Slenders,[1] Eleonora Perego,[1] Mauro Buttafava,[2] Giorgio Tortarolo,[1] Enrico Conca,[2] Sabrina Zappone,[1] Agnieszka Pierzynska-Mach,[3] Federica Villa,[2] Enrica Maria Petrini,[4] Andrea Barberis,[4] Alberto Tosi,[2] and Giuseppe Vicidomini[1,*]

[1]Molecular Microscopy and Spectroscopy, Istituto Italiano di Tecnologia, Genoa, Italy; [2]Dipartimento di Elettronica, Informazione e Bioingegneria, Politecnico di Milano, Milan, Italy; [3]Nanoscopy & NIC@IIT and [4]Synaptic Plasticity of Inhibitory Networks, Istituto Italiano di Tecnologia, Genoa, Italy

ABSTRACT   The single-photon timing and sensitivity performance and the imaging ability of asynchronous-readout single-photon avalanche diode (SPAD) array detectors have opened up enormous perspectives in fluorescence (lifetime) laser scanning microscopy (FLSM), such as super-resolution image scanning microscopy and high-information content fluorescence fluctuation spectroscopy. However, the strengths of these FLSM techniques depend on the many different characteristics of the detector, such as dark noise, photon-detection efficiency, after-pulsing probability, and optical cross talk, whose overall optimization is typically a trade-off between these characteristics. To mitigate this trade-off, we present, to our knowledge, a novel SPAD array detector with an active cooling system that substantially reduces the dark noise without significantly deteriorating any other detector characteristics. In particular, we show that lowering the temperature of the sensor to $-15°C$ significantly improves the signal/noise ratio due to a 10-fold decrease in the dark count rate compared with room temperature. As a result, for imaging, the laser power can be decreased by more than a factor of three, which is particularly beneficial for live-cell super-resolution imaging, as demonstrated in fixed and living cells expressing green-fluorescent-protein-tagged proteins. For fluorescence fluctuation spectroscopy, together with the benefit of the reduced laser power, we show that cooling the detector is necessary to remove artifacts in the correlation function, such as spurious negative correlations observed in the hot elements of the detector, i.e., elements for which dark noise is substantially higher than the median value. Overall, this detector represents a further step toward the integration of SPAD array detectors in any FLSM system.

WHY IT MATTERS   Single-photon avalanche diode array detectors are revolutionizing fluorescence laser scanning microscopy. Thanks to their single-photon timing and sensitivity ability and their imaging faculty, a single-photon avalanche diode array detector transforms any fluorescence laser scanning microscopy into a super-resolution microscope and opens a whole range of possibilities for the study of sample dynamics by means of fluorescence fluctuation spectroscopy (FFS). However, dark noise can be a severe problem for both imaging and FFS. For imaging, the signal overcomes noise only for a relatively high illumination intensity, which can be detrimental for live-cell experiments. For FFS, the noise leads to artifacts in the correlation curves, potentially leading to wrong conclusions about the sample. We show that lowering the temperature of the detector to $-15°C$ solves both problems.

INTRODUCTION

Fluorescence laser scanning microscopy (FLSM) is one of the most powerful experimental tools in life sciences thanks to its ability to observe (sub)cellular structures

and biomolecular processes under physiological conditions (1,2). Together with many other technical aspects, the choice of the detector is crucial to exploit the full potential of FLSM or to implement a specific FLSM technique (e.g., imaging, fluorescence fluctuation spectroscopy (FFS), and their combinations with fluorescence lifetime measurements).

For FLSM-based FFS, single-photon avalanche diodes (SPADs) are desirable. FFS is a family of techniques able to measure the mobility of and interactions between (bio)molecules (3). These methods rely on

measuring fluctuations in the fluorescence intensity arising from a population of biomolecules passing through the FLSM probing (or detection) volume. Because of the low photon fluxes typically observed in these experiments—the fluorescence signal is generated from only a few fluorophores at a time—the single-photon sensitivity of SPADs is very important. Furthermore, SPADs allow recording the single-photon signal with a temporal precision (photon-timing precision) of tens of picoseconds with respect to a reference event—usually the pulsed laser excitation event; thus, these detectors are ideal for time-correlated single-photon counting (TCSPC), which is the basis for fluorescence lifetime measurements and other time-resolved experiments. For FLSM-based imaging, photomultiplier tubes (PMTs) are preferable to SPAD detectors because of the higher dynamic range (4). After recording a photon, the SPADs are blind for a fixed period of time (typically, 20–200 ns), the so-called hold-off time or dead time. Hence, SPADs have a maximal photon count rate limited by the inverse of the hold-off time (5–50 MHz) (5). Furthermore, the detector response becomes nonlinear at photon fluxes already much lower than the maximal photon count rate. On the other hand, although PMTs offer a superior linearity at high photon fluxes, they are not ideal for either FFS or fluorescence lifetime applications. Indeed, PMTs have a lower photon sensitivity than SPADs, and the digitization of the analog PMT output, required for the TCSPC recording, may introduce unwanted fluctuations in the signal and lead to a worse photon-timing precision compared with SPADs (6).

Because of the growing interest in FLSM systems that can do both imaging and FFS, the last years have shown the development of new detectors that combine the best characteristics of PMTs and SPADs. Hybrid detectors (HyDs) have been designed to achieve a high dynamic range, high photon sensitivity, and good photon-timing precision. In the context of FFS, the high dynamic range supports experiments with a wide range of (bio)molecular concentrations (7). However, the complexity needed to achieve these specifications and the use of a photocathode (as for PMTs) reduces the robustness of the HyDs with respect to solid-state devices, such as SPADs: SPADs are immune to magnetic fields, highly resistant to mechanical shocks, and do not suffer from "burn-in" by incidental light saturation. Silicon photomultipliers (SiPMs), also called multipixel photon counters, are solid-state alternatives with a high dynamic range. An SiPM is an array of microcells, each having a SPAD and a quenching resistor, characterized by a single analog output obtained by summing the signals of all pixels. The large number of elements in the array allows many photons to be detected simultaneously without saturation (8).

Because an SiPM is an asynchronous read-out detector (i.e., it provides an analog current every time one or more SPADs get triggered), it can also be used for photon counting and for TCSPC experiments, providing a proper signal elaboration. The elaboration is easy for photon counting but more complex for TCSPC. Indeed, it is necessary to temporally separate the signals from two or more photons arriving quasisimultaneously. This task can be achieved efficiently by combining SiPMs with the HyD technology (9).

Even though SiPM is a pixelated detector, it provides, similar to HyD, SPAD, and PMT detectors, a single output: the spatial information of where photons hit the sensor's active area (in the case of SiPM, which SPAD element of the array) is lost. However, it has recently been shown that having access to this spatial information can shine new light on FLSM. Indeed, by using an array of detectors to image the probing volume of the FLSM, it is possible to reconstruct super-resolved images via the image scanning microscopy (ISM) concept (10–14). Furthermore, when the detector array also provides a high temporal resolution (more than one megahertz), the combined spatiotemporal information can be used to augment the information content provided by a single FFS experiment (15,16), i.e., the so-called comprehensive correlation analysis. The same spatiotemporal information combined with a similar correlation analysis was used to implement nanoscopy imaging (17). Finally, by combining the spatial and timing information, super-resolution fluorescence lifetime imaging (14) and nanoscopy techniques based on photon coincidences (quantum microscopy) become feasible (18).

Asynchronous read-out SPAD array detectors solve the problem of SiPM while maintaining the best features of all other FLSM detectors (19). Similarly to SiPM, these detectors are composed of an array of SPADs, but each SPAD can be read independently from the others. The possibility to implement such a read-out scheme is a consequence of the fact that imaging the probing region of an FLSM requires only a few tens of SPADs (e.g., 5×5 up to 7×7) and not a million of elements as for wide-field microscopy imaging. It is worth noting that SPAD array cameras with a much higher number of elements are well established (20). However, to efficiently transfer the enormous amount of spatiotemporal information, they typically implement synchronous read-out (i.e., frame by frame), and they implement the photon counting or the TCSPC features on the detector itself, thus reducing the versatility of the system (20). Because each SPAD element provides a single digital pulse each time a photon is registered, the asynchronous read-out SPAD array maintains all the characteristics of single-element SPAD detectors, such as a high sensitivity, optimal photon-timing

precision, and no read-out noise. Furthermore, as for SiPM, the multiple element architecture improves the dynamic range.

However, to effectively revolutionize FLSM, asynchronous read-out SPAD array detectors need to display excellent performance also on other important characteristics, such as photon-detection efficiency (PDE), optical cross talk probability, after-pulsing probability, and dark noise. For SPAD arrays, the PDE depends both on the quantum efficiency of the SPAD and the fill factor of the array (i.e., the ratio of its sensitive area to its total area). Typically, the higher the fill factor, the higher the cross talk probability (i.e., the probability of an element to register a photon event as a consequence of a photon event in an adjacent element). The use of microlenses is therefore a desirable alternative to increase the fill factor. In parallel, we have recently shown that the quantum efficiency of a SPAD array can be improved by using the Bipolar-complementary metal−oxide−semiconductor (CMOS)-double diffused metal oxide semiconductor (BCD) fabrication technology instead of the more traditional CMOS technology (21,22). Indeed, BCD SPAD detectors offer superior quantum efficiency, a low after-pulsing probability, excellent photon-timing precision, and a low cross talk. These features come at the price of a higher dark count rate (DCR; i.e., the rate of spurious avalanche events due to carriers generated within the detector in the absence of light) and a higher probability of "hot pixels" (i.e., elements whose DCR is significantly higher than the average of the array) (22). The DCR in a SPAD array detector can be decreased by reducing the active area of the SPAD but at the cost of a reduced fill factor. An alternative approach with negligible detrimental effects is reducing the operating temperature of the SPAD: cooling down silicon SPADs reduces the DCR by about a decade for every $20°C$ of temperature reduction (23).

In this work, we implemented an active cooling system integrated in our BCD SPAD array detector. We demonstrated that operating the cooling system at $-15°C$ reduces the DCR by more than one order of magnitude, with a negligible increase of the after-pulsing probability, and no effect on the cross talk probability. We then integrated the cooled SPAD array detector in an FLSM system, and we show the substantial enhancement obtained both in the context of imaging and FFS. We performed imaging of fixed and live cells, and we investigated the diffusion of freely diffusing beads in aqueous suspension and green fluorescent protein (GFP)-tagged proteins in living cells. These experiments demonstrated that the cooled detector allows 1) reducing the illumination power, or equivalently the pixel dwell time, to achieve a high signal/noise ratio (SNR) and the resolution predicted by ISM, and 2) removing the artifacts introduced in FFS experiments by the dark noise, thus obtaining sound and robust molecule mobility information. This issue makes ISM among the most gentle super-resolution techniques for live-cell investigations. We believe that this work represents an important step toward the integration of SPAD array detectors in any FLSM and, more in general, a significant contribution to the so-called single-photon revolution: fluorescence photons from the sample are collected one by one with a series of signatures (e.g., in time and space), whose analysis can generate, to our knowledge, new insights about the sample, otherwise lost by conventional light recording.

MATERIALS AND METHODS

Cooling system

To reduce the DCR of the 5×5 BCD SPAD array detector described in (22), and thus to fully exploit the PDE enhancement (with respect to the CMOS-based counterpart (22)), we designed a compact electro-mechanical system capable of effectively cooling the device while keeping it compatible with the existing FLSM setup. The dimensions of the overall assembly are $50 \times 50 \times 23$ mm.

A two-piece-machined aluminum chamber (baseplate and cover) was designed to hermetically isolate the device from the environment, thus avoiding water condensation on cold surfaces and minimizing the heat exchange between the sensor and its environment (Fig. 1). The SPAD array chip, with a size of 1.3×1.2 mm, was directly mounted onto a custom-made miniature two-stage thermoelectric cooler (TEC), manufactured by Ferrotec (Santa Clara, CA). This TEC has a maximal heat transfer power of 1.1 W and a maximal temperature difference between cold and hot sides of $95°C$. The sensor chip is glued onto the TEC cold plate using a thermo-conductive silver-loaded epoxy resin (Master Bond, Hackensack, NJ), whereas the same glue is also used to attach the TEC hot side to the chamber baseplate, which acts as the overall heat sink. The temperature sensing was done using a negative temperature coefficient (NTC) resistor with wire-bonding pads (FTN18XH103F01RT; Murata Manufacturing, Kyoto, Japan) glued onto the TEC cold plate. The aluminum chamber hosts a printed circuit board (PCB) needed to route the electrical signals to the acquisition board through an external connector and a high-density flat-flex cable. It also hosts surface-mount, decoupling capacitors for the sensor power supply rails. This four-layer special PCB is made by hydrocarbon ceramic laminates (4350B; Rogers, Chandler, AZ), which exhibits a lower hygroscopy compared with classical fiberglass materials. Connections between the PCB, sensor, and NTC resistor are made through 25-μm-diameter bonding wires. Fluorescence photons can reach the sensor through an antireflection coated glass window (WG11010-A; ThorLabs, Martinsried, Germany). The antireflection window is glued to the chamber cover using a vacuum-grade epoxy resin (TorrSeal; Agilent, Santa Clara, CA). The same epoxy resin is also used to hermetically close the gap of the PCB exiting the chamber baseplate. The two pieces of the chamber are sealed using a vacuum-grade o-ring and six M2 screws, allowing for future replacement or upgrade of the sensor if needed. The internal volume of the chamber was filled with argon gas after a baking procedure of 3 h at $60°C$ under light vacuum to remove any internal residual moisture.

TEC control and temperature stabilization are performed using a dedicated integrated circuit (MAX1978; Maxim, San Jose, CA) with a negative feedback loop ensuring a stability better than $0.1°C$. An eight-bit microcontroller (PIC18; Microchip Technology, Chandler,

A

Cover — Glass — SPAD array — O-ring

PCB — Baseplate — TEC — Temperature sensor

B
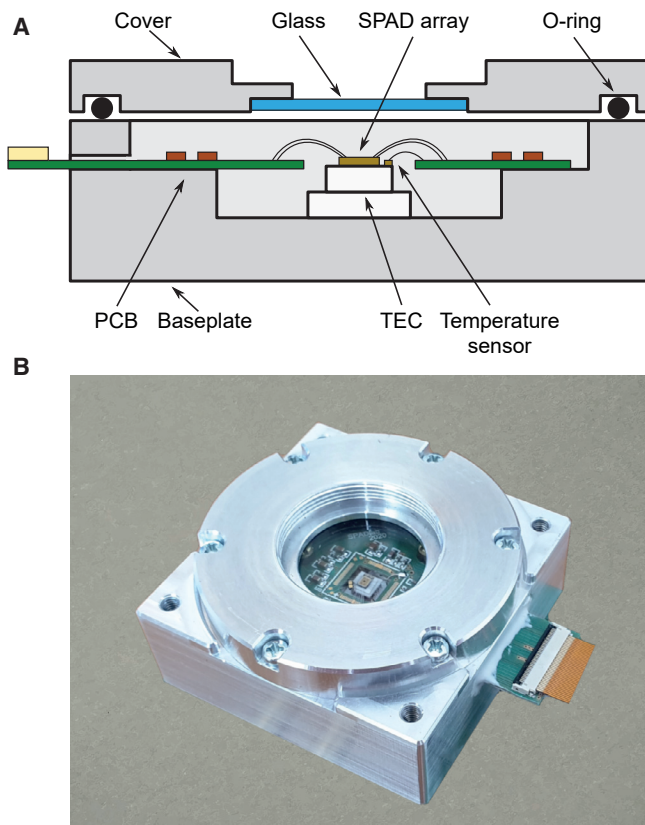
FIGURE 1   Cooled 5 × 5 SPAD array sensor. (*A*) Simplified cross section of the 5 × 5 SPAD array assembly, mounted into the cooling aluminum chamber. The sensor chip was directly glued on a two-stage TEC, floating from surrounding objects. Operating temperature is measured using an NTC resistor. Electrical connections to the chip were implemented through 25-μm bonding wires, thus minimizing heat transfer, and then transferred to an internal PCB and to a high-density flat-flex connector. The entire chamber was hermetically sealed and filled with argon gas to avoid condensation and to further decrease heat exchange. Photons can reach the sensor through a 1-inch antireflection-coated glass window. (*B*) Picture of the assembled sensor.

AZ) is responsible for setting and monitoring the system parameters and communicates with the host personal computer through a Universal Serial Bus 2.0 link. Detector supply and control are performed using the same electronic boards previously described in (22). Operating temperatures ranging from room temperature (RT) down to $-15°C$ can be chosen, whereas the sensor bias voltage must be adjusted accordingly to maintain a constant excess bias voltage of 5 V (22). For the data presented here, the detector hold-off time (dead time) was set to 100 ns, which is a good trade-off between a low after-pulsing probability and a high maximal count rate.

Microscope

The microscopy setup used both for imaging and FFS in this work is similar to the setup extensively described in (16), except for the new detector assembly. In short, a 485-nm, 80-MHz-pulsed laser is reflected by a dichroic beam splitter and galvanometric scanning mirrors, then sent through a Leica scan lens/tube lens system (Wetzlar, Germany) and finally focused onto the sample by a 100×/1.4 Leica oil immersion objective. The fluorescence signal is collected in descanned mode, passing through the dichroic beam splitter, a 488-nm

notch filter and a band-pass 500-550 nm emission filter (ZEISS, Oberkochen, Germany). The fluorescence is finally focused onto the detector photosensitive area, with a back-projected size at the sample plane of 1.5 Airy units. We measured all the laser power values at the back-aperture of the objective lens.

We controlled the microscope with the BrightEyes control and data-acquisition module (BrightEyes-CDAQM), a home-built LabVIEW (National Instruments, Austin, TX) program based on the Carma application (Genoa Instruments, Genoa, Italy) (24,25). The Bright-Eyes-CDAQM uses a field-programmable-gate-array-based data-acquisition card (NI USB-7856R; National Instruments), which guarantees fast prototyping and great flexibility. In short, the Bright-Eyes-CDAQM 1) provides a graphical user interface to control the major acquisition parameters (e.g., scanned region, pixel size, pixel dwell time, (*x*, *y*) coordinates for the fluorescence correlation spectroscopy (FCS) measurement); 2) registers (in photon-counting mode) the 25 digital signals of the detector array in temporal bins of minimal 500 ns and in synchronization with the beam scanning system and other devices, e.g., laser shutters; and 3) visualizes the recorded signals (e.g., intensity images and time traces). A quite unique feature of the BrightEyes-CDAQM is the possibility to record, for each pixel, the fluorescence signal over multiple temporal bins, resulting in a four-dimensional photon-counting (intensity) data structure $I(t, x, y, c)$, where t is the time course within the pixel dwell time, (*x*, *y*) are the spatial scanning coordinates, and c is the element or channel of the SPAD array detector. For FFS, the software records a photon-counting time series for each SPAD array channel, i.e., $I(t, c)$, where t are the 500-ns temporal bins. The BrightEyes-CDAQM stores both FFS and image data in HDF5 files.

Samples

Fixed beads

Yellow-green carboxylate FluoSpheres (catalog number F8803, 2% solids, 100-nm diameter, exc./em. 505/515 nm; Invitrogen, Thermo Fisher Scientific, Waltham, MA) were diluted 1000× in ultrapure water and sonicated for 10 min in a water bath sonicator (Labsonic LBS1−0.6; FALC Instruments, Treviglio, Italy). 100 μL of the suspension was poured onto a coverslip previously coated with a poly-L-lysine solution (0.01%). After 8 min, the residue was removed, and the coverslip was mounted on a microscope slide with a mounting buffer.

Beads in suspension

Yellow-green carboxylate FluoSpheres (catalog number F8787, 2% solids, 20-nm diameter, actual size 27 nm, exc./em. 505/515 nm; Invitrogen, Thermo Fisher Scientific) were diluted 5000× in ultrapure water at RT. Before each measurement, the bead solution was sonicated for 10 min in a water bath sonicator (Labsonic LBS1−0.6; FALC Instruments). A droplet of the bead solution was poured onto a coverslip for the FFS measurements.

Fixed cells

HeLa cells were cultured in Dulbecco's Modified Eagle Medium (Gibco, Thermo Fisher Scientific) supplemented with 10% fetal bovine serum (Sigma-Aldrich, Steinheim, Germany) and 1% penicillin-streptomycin (Sigma-Aldrich) at 37°C in 5% CO_2. 1 day before immunostaining, the cells were seeded onto coverslips in a 12-well plate (Corning, Corning, NY). Cells were incubated in a solution of 0.3% Triton X-100 (Sigma-Aldrich) and 0.1% glutaraldehyde (Sigma-Aldrich) in the BRB80 buffer (80 mM PIPES, 1 mM EGTA, and 4 mM MgCl (pH 6.8); Sigma-Aldrich) for 1 min. HeLa cells were fixed with a solution of 4% paraformaldehyde (Sigma-Aldrich) and 4% sucrose (Sigma-Aldrich) in the BRB80 buffer for 10 min and then washed three times for 15 min in phosphate-buffered saline (PBS; Gibco, Thermo Fisher Scientific). Next, cells were treated

for 10 min with a solution of 0.25% Triton X-100 in blocking buffer (solution of 3% bovine serum albumin (Sigma-Aldrich) in BRB80 buffer), and washed three times for 15 min in PBS. After 1 h in blocking buffer, HeLa cells were incubated with monoclonal mouse anti-α-tubulin antibody (Sigma-Aldrich) diluted in the blocking buffer (1:1000) for 1 h at RT. The anti-α-tubulin antibody was revealed with anti-mouse Alexa Fluor 488 (Invitrogen, Thermo Fisher Scientific). HeLa cells were rinsed three times in PBS for 15 min. Finally, the coverslips were mounted onto microscope slides (Avantor, VWR International, Milano, Italy) with ProLong Diamond Antifade Mountant (Invitrogen, Thermo Fisher Scientific).

Live cells

HEK293T cells were cultured in Dulbecco's Modified Eagle's Medium (Gibco, Thermo Fisher Scientific) supplemented with 1% Minimum Essential Medium, Non-Essential Amino Acid Solution (Sigma-Aldrich), 10% fetal bovine serum (Sigma-Aldrich), and 1% penicillin-streptomycin (Sigma-Aldrich) at 37°C in 5% CO_2. HEK293T cells were seeded onto a μ-Slide 8 Well plate (Ibidi, Gräfelfing, Germany). HEK293T cells were co-transfected with super-ecliptic-pHluorin (SEP)-tagged-β3 subunit gamma-aminobutyric acid, type A ($GABA_A$) receptor, a pH-sensitive variant of GFP (26,27), and α1 subunit $GABA_A$ receptor (28) to form functional $\alpha\beta$ $GABA_A$ receptors, for the live-cell time-lapse experiment and with pcDNA3.1(+)enhanced GFP (eGFP; Addgene plasmid #129020) for the FFS measurements. Transfection was performed using Lipofectamine 3000 Transfection Reagent (Invitrogen, Thermo Fisher Scientific) according to manufacturer's protocol. U2-OS cells stably expressing eGFP-DEK fusion protein were cultured in McCoy's 5a modified medium (Thermo Fisher Scientific) supplemented with 10% fetal bovine serum (Sigma-Aldrich) and 1% penicillin-streptomycin (Sigma-Aldrich) at 37°C in 5% CO_2. Cells were seeded on a μ-Slide 8-Well plate Glass Bottom (n. 80827; Ibidi) 48 h before the measurement. Measurements were performed in Live Cell Imaging Solution (Thermo Fisher Scientific) at RT.

Imaging

Fixed beads

We recorded bead images of 512 × 512 pixels, with a pixel size of 39 nm and a pixel dwell time of 100 μs. We split each data set into two time bins of 50 μs each. All photons arriving during the first 50 μs were used to build a first image and likewise for the second image. We used the two images to evaluate the effective resolution by means of the Fourier ring correlation (FRC) analysis.

Fixed cells

We recorded cell images of 1500 × 1500 pixels, with a pixel size of 50 nm and a pixel dwell time of 50 μs, divided into 100 time bins of 500 ns each. Images were taken with the SPAD array detector at RT and at −15°C.

Live cells

We recorded live-cell images of 1000 × 1000 pixels with a pixel size of 55 nm and a dwell time of 30 μs per pixel at RT. The laser power was 12 μW. One single image was acquired approximately every 3 min, for a total time of 1 h of total acquisition. We reconstructed all the super-resolved images, as described in the section below.

Image reconstruction and analysis

We processed the imaging data set with the Miplib library in Python (29,30). The Miplib library contains the adaptive pixel reassignment method for ISM reconstruction (14) and the FRC analysis for the eval-uation of the image effective spatial resolution (29,31). The FRC analysis typically requires two "identical" images, which we obtained by using the ability of the BrightEyes-CDAQM to temporally split the fluorescence signal of each pixel in different time windows— within the pixel dwell time. To compare the resolution as a function of the excitation laser power, we divided the pixel dwell time into two identical time windows, yielding the intensity data sets, $I^1(x, y, c)$ and $I^2(x, y, c)$. For each data set, we reconstructed the relative Sum 5 × 5 images and adaptive pixel reassignment ISM images, which can be used for the FRC analysis.

To compare the resolution as a function of the pixel dwell time, we measured for each pixel the fluorescence signal over a time interval of 50 μs, divided in time bins of 500 ns each, yielding 100 images of the sample. These were combined in postprocessing to generate pairs of images with increasing pixel dwell times. For each dwell time Δt between 500 ns and 25 μs (in steps of 500 ns), we generated two independent images, $I^1(x, y, c, \Delta t)$ and $I^1(x, y, c, \Delta t)$, by summing the first $N = \Delta t/500$ ns odd-numbered and even-numbered images of the time series, respectively. For each pair I^1 and I^2, we calculated the Sum 5 × 5 and the ISM reconstructed images, and we applied the FRC algorithm.

FFS

Beads in suspension

For beads measurements, a droplet of a freshly made bead suspension was poured onto a coverslip. Five measurements of at least 300 s each were performed with a laser power of 6.4 μW for a detector temperature of −15°C and at RT. The acquired time traces of the different configurations (such as $I_{12}(t)$, $I_{Sum3 \times 3}(t)$, $I_{Sum5 \times 5}(t)$, etc.) were split into chunks of 10 s, and the autocorrelation of each chunk was calculated using the Multipletau Python package (32). Afterwards, all chunks from each time trace were averaged. Correlations were calculated for logarithmically scaled lag times ranging from 500 ns to 0.1 s. For scanning FCS, the fluorescence time trace was recorded while scanning the laser beam in circles of 0.5 μm in diameter with a frequency of 320 μs per circle by using the galvanometric scanning mirrors. For a scan speed that is fast (compared with the sample dynamics), scanning FCS allows extracting both the beam waist and the diffusion coefficient from a single measurement (33) (Supporting materials and methods, Note S1). The technique can thus be considered a calibration-free alternative of conventional FCS.

Live cells

HEK293T or U2-OS eGFP-DEK cells were placed on the microscope stage in a μ-Slide 8 Well plate (Ibidi) with Live Cell Imaging Solution (Thermo Fisher Scientific). The BrightEyes-CDAQM allows imaging of a sample, after which the user can choose the positions for FFS measurements by simply clicking on the image. Multiple FFS measurements of at least 90 s each, in different cells and in different positions within each cell, were performed with a laser power of 12 μW, for a detector temperature of −15°C and at RT. The acquired intensity time traces of the different configurations ($I_c(t)$ with c the SPAD array element, $I_{Sum3 \times 3}(t)$ and $I_{Sum5 \times 5}(t)$) were split into chunks of 10 s, and the autocorrelation of each chunk was calculated using the Multipletau Python package (32), as for the beads measurements. Afterwards, all chunks from each time trace were averaged, discarding time traces that showed clear photobleaching. The measurements performed on the eGFP-expressing cells and in the cytoplasm of U2-OS eGFP-DEK-expressing cells were fitted with a one component FCS model, whereas for the measurements on the eGFP-DEK in the nuclei, a model with anomalous diffusion was considered (see Supporting materials and methods, Note S1). The least-squares optimizer of the SciPy library was used to fit all the correlation curves.

RESULTS AND DISCUSSION

Detector characterization

We first compared the main characteristics of the SPAD array detector as a function of the temperature by implementing a series of experiments on a test bench. To evaluate the reduction of the DCR as a function of the temperature, we placed the detector in a light-tight box, and we measured the number of counts per unit of time. In the "hottest" SPAD element, the DCR decreases more than 10 times: from 18.8 kHz at 25°C to 1.6 kHz at −15°C. In the central element (i.e., element 12), which is the element that typically receives the most photons in any imaging or FFS experiments, the DCR decreases more than 20 times: from 2.2 to 0.1 kHz (Fig. 2 A). Despite the substantial reduction, a value of 0.1 kHz is still higher than expected: indeed, we expected a reduction of two orders of magnitude with a temperature change of −40°C. This apparent deviation is a consequence of the cross talk effect: we repeated the experiment at −15°C by sequentially keeping only one element on at a time and found that the DCR for the central element decreases to 0.01 kHz, thus confirming the expected reduction of two orders of magnitude (Fig. 2 B).

It is well known that reducing the temperature of the SPAD array can increase the after-pulsing probability (34): the main source for after-pulses are trapped charges that are released over time, and the lifetime of the traps typically becomes longer for lower temperatures. To monitor the effect of the temperature on the after-pulsing probability, we recorded with the BrightEyes-CDAQM the intensity time traces produced by the detector when illuminated uniformly by an uncorrelated source, such as a light-emitting diode. We then calculated the autocorrelation functions multiplied by the average intensity (in the range 2−35 kHz) to take into consideration the DCR variation (35). The curves clearly show a correlation at short lag times (below one microsecond), which are induced by the after-pulsing effect (Fig. 2 C). Because the BrightEyes-CDAQM has a time resolution of 500 ns, we implemented the same experiment with a different data-acquisition system to quantify the increase in after-pulsing probability as a function of the temperature (22). In particular, we used a TCSPC to measure the interarrival times between consecutive output pulses of an individual pixel. The contribution of the DCR to the interarrival times histogram can be fitted with an exponential decay at long interarrival times and then subtracted from the experimental data to have only the contribution of avalanches from the after-pulses. The after-pulse probability is then computed as the integral sum of the after-pulsing events, divided by the integral sum of the histogram itself (i.e., the total number of avalanches) (Fig. 2 D). By reducing the temperature from 25°C down to −15°C, the after-pulsing probability increases from 0.27 to 0.42%, but remains relatively low, being fully compatible with FFS.

To quantify the effect of the temperature on the optical cross talk between the SPAD array elements, we
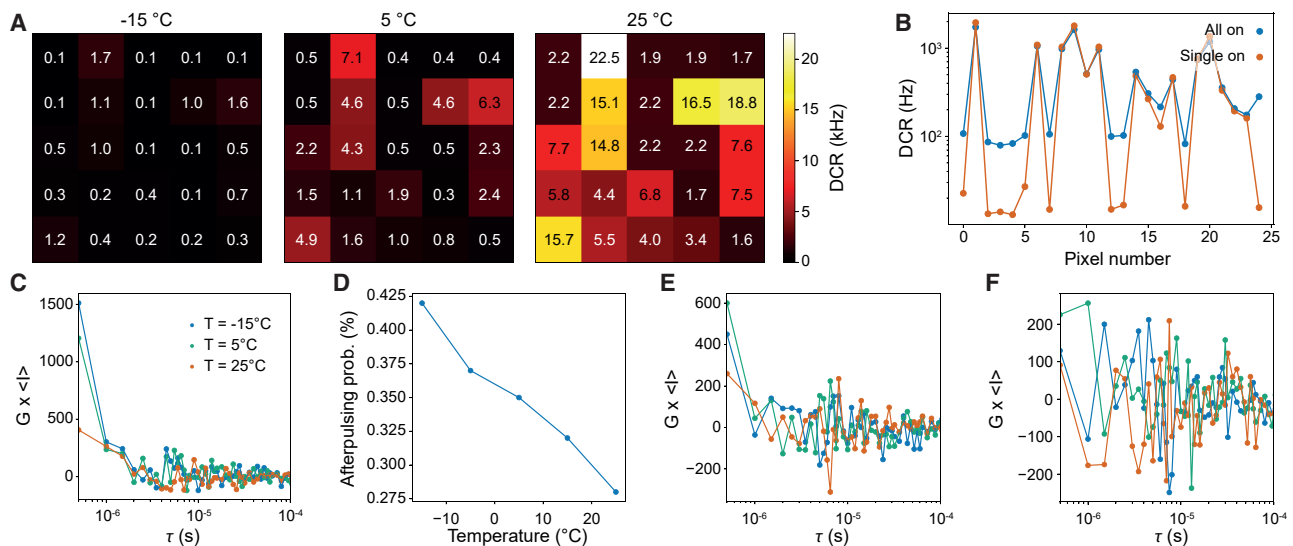

FIGURE 2 Specifications of the SPAD array sensor. (A) Dark count rate (DCR) for each pixel for various detector temperatures. The DCR was measured with all pixels simultaneously turned on. (B) Comparison between the DCR measured with all pixels simultaneously turned on (*All on*) and all pixels sequentially turned on (*Single on*) for a detector temperature of −15°C. (C) Normalized autocorrelation of the central pixel under noncorrelating ambient light for different detector temperatures. (D) After-pulsing probability as a function of the detector temperature for the central pixel. (E and F) Averaged and normalized cross correlations between the central pixel and the four nearest orthogonal neighbors (E) or the four nearest diagonal neighbors (F) under ambient light. Same colors as in (C).

used the same setup with the BrighEyes-CDAQM as for the after-pulsing characterization. However, instead of calculating the autocorrelation, we calculated the cross correlation between adjacent elements. Neither the correlation curves between orthogonal neighbors nor between diagonal neighbors show substantial changes as a function of the temperature (Fig. 2, *E and F*), thus demonstrating that by cooling the detector the optical cross talk probability does not degrade.

In short, cooling the BCD SPAD array to −15°C drastically decreases the DCR without substantially worsening any other characteristics, such as the after-pulsing probability and the optical cross talk. Notably, by cooling this detector to −15°C, the DCR performance becomes similar to our CMOS SPAD array detector (14,16,29), which is, to the best of our knowledge, the only SPAD array detector effectively used so far to implement both ISM and comprehensive correlation analysis. On top of this, our BCD SPAD array offers superior characteristics in terms of PDE and after-pulsing probability (22).

Imaging

To demonstrate the benefits of the cooled SPAD array detector in terms of imaging, we first used a calibration sample composed of 100-nm fluorescent beads. We compared imaging of beads acquired with the detector running at RT (uncooled) and at −15°C (cooled) for a series of different excitation laser powers (Fig. 3). For a relatively high laser power (920 nW), cooling the detector has a relatively small effect on the image quality. The contribution of the dark noise to the overall fluorescent signal is low. As a result, the images made with the cooled and uncooled detector look very similar, and the FRC analysis (Fig. 3, *B−D*) reveals only a minor improvement in the ISM resolution upon cooling. However, for lower laser powers, the image quality with the uncooled detector deteriorates quickly. With 70 nW, the beads hardly protrude above the noise level, and the FRC resolution drops by 53% from ∼200 nm at 920 nW to more than 300 nm at 70 nW. Lowering the laser power also negatively affects the resolution of images taken with a cooled detector, but in this case, the
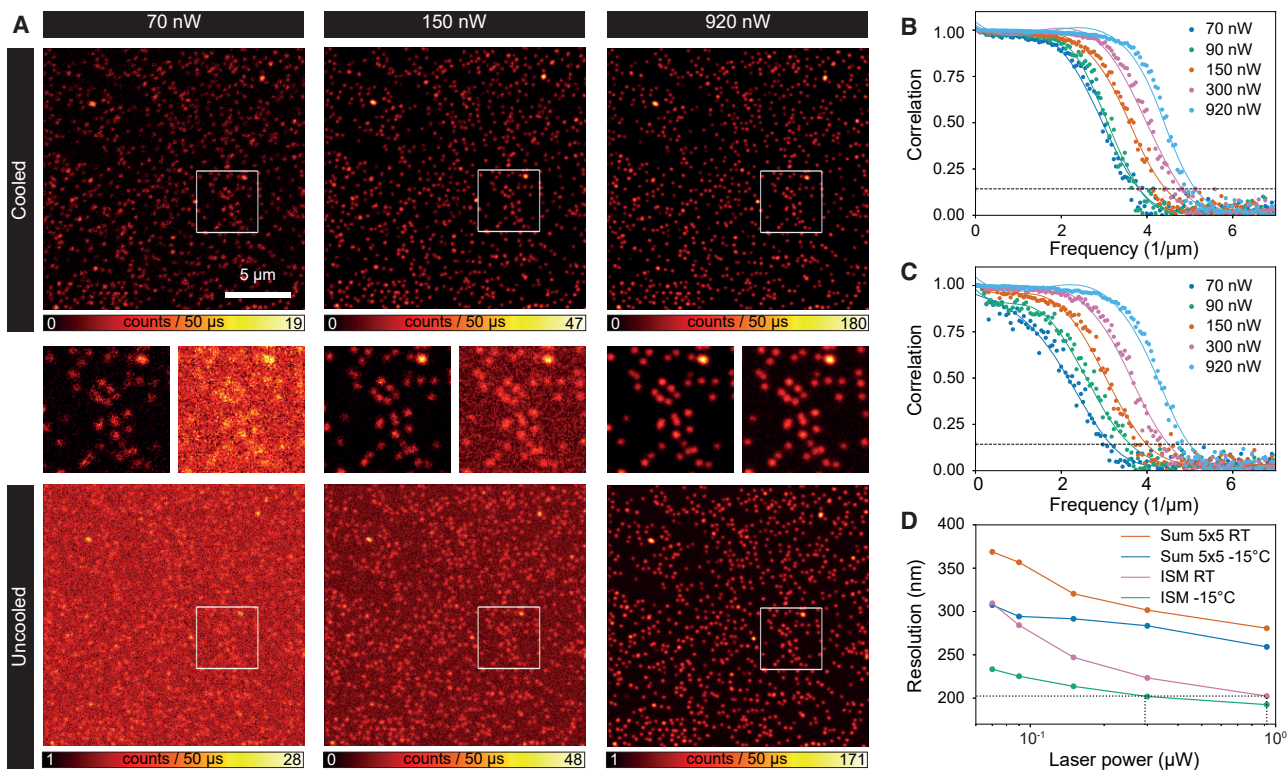

FIGURE 3 Comparison imaging fixed beads with a cooled (−15°C) versus uncooled (25°C) SPAD array detector. Shown is a sample of 100-nm yellow-green beads. Laser powers were measured at the back focal plane of the objective and are average powers of an 80-MHz pulsed laser. (*A*) Example of some of the ISM images. The indicated square regions of length 4.7 μm are shown enlarged in the middle row (*left*: cooled; *right*: uncooled). (*B and C*) FRC curves for cooled (*B*) and uncooled (*C*) imaging for various laser powers. The corresponding values for the resolution (*D*) were calculated from the intersection of the FRC curves with the indicated horizontal line at $y = 1/7$. (*D*) FRC resolution as a function of the laser power for the cooled (−15°C) and uncooled (room temperature (RT)) detector. Curves for both confocal imaging (*Sum* 5 × 5) and ISM are plotted. The same ISM resolution at RT with a laser power of 920 nW is reached with a cooled detector with only 294 nW (linear interpolation), represented by black lines.

difference is only 21% from ~192 nm at 920 nW to 233 nm at 70 nW. Cooling the detector allowed lowering the laser power by more than a factor of three without sacrificing the resolution (Fig. 3 D). This result clearly illustrates the importance of cooling the detector for long-term live-cell imaging, in which phototoxicity and photobleaching effects come into play.

Alternatively, a cooled detector can be used to either decrease the laser power or to increase the imaging speed while maintaining the SNR and thus the resolution obtained with an uncooled detector. To validate this claim, we compared the FRC-based resolution between cooled and uncooled detector imaging of fixed HeLa cells as a function of the pixel dwell time (Fig. 4). We performed the comparison both for confocal and ISM imaging. As expected, for all the imaging conditions tested (i.e., confocal, ISM, cooled, and uncooled), the resolution improves for increasing pixel dwell times. Notably, the ISM resolution at RT (25°C) decreases faster than the confocal microscopy resolution at −15°C. Consequently, for long enough pixel dwell times, i.e., high enough SNRs, ISM at RT performs better than confocal microscopy with a cooled detector. However, when comparing confocal microscopy with a cooled or uncooled detector or ISM with a cooled or uncooled detector, it is clear that cooling

the detector allows reducing the pixel dwell time by more than a factor of two while maintaining the resolution obtained with an uncooled detector.

Finally, we used the cooled SPAD array detector on living cells, performing a time-lapse video of cells co-expressing the (SEP)-tagged-$\beta 3$ and the $\alpha 1$ subunit of the GABA$_A$ receptor, which co-assemble to form functional pentameric GABA$_A$ receptors expressed at the membrane surface. These receptors are known to mediate the main source of synaptic inhibition in the central nervous system. Despite the relatively low laser power (12 μW), we obtained high contrast and high SNR images by cooling the detector. We imaged the same cell for more than 1 h, and we did not observe any sign of phototoxicity or photobleaching (Fig. S3; Video S1).

FFS

To demonstrate the benefits of our—to our knowledge—new cooled SPAD array detector in the context of FFS, we performed spot-variation (or diffusion law) FCS, a technique in which the transit time is measured as a function of the detection volume size. In particular, we compared the results of spot-variation FCS experiments performed at different detector temperatures
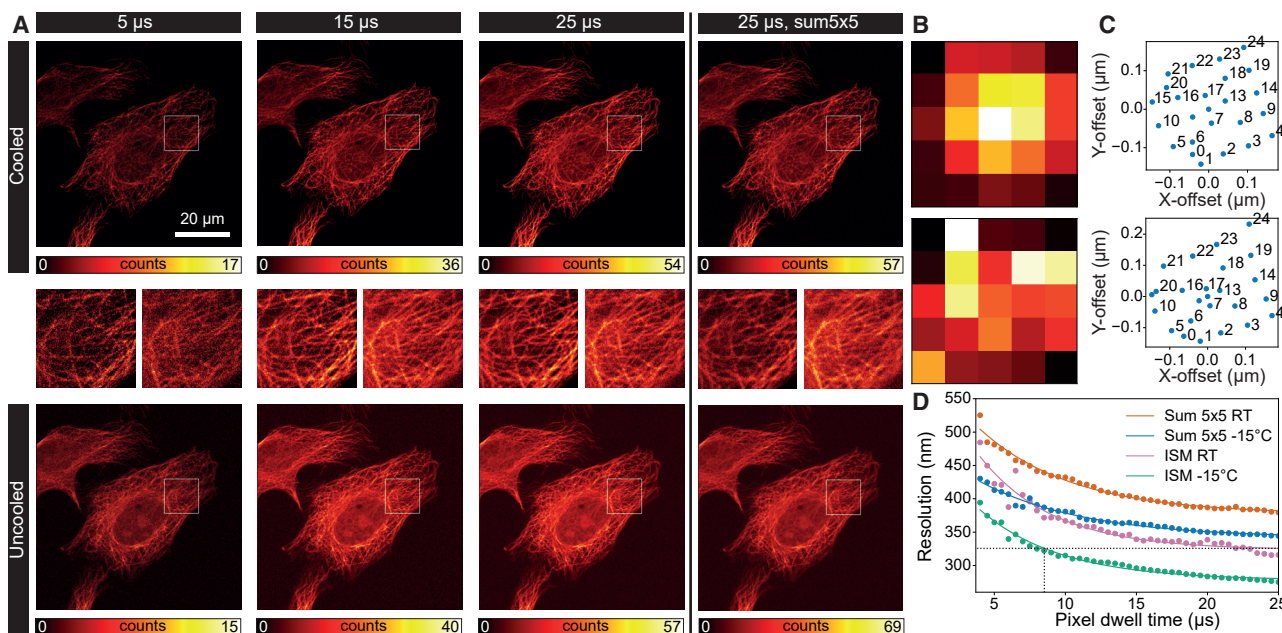
FIGURE 4 Comparison cooled versus uncooled SPAD array detector for different pixel dwell times in images of fixed HeLa cells with α-tubulin staining. Laser power was 100 nW at the back focal plane of the objective. The SPAD array detector was cooled down to −15°C or used at RT or uncooled, respectively. (A) ISM images for various pixel dwell times and comparison with the *Sum* 5 × 5 image for a pixel dwell time of 25 μs. The middle row shows zoomed-in images of the indicated square regions of length 12.5 μm of the top row images (*left*) and the bottom row images (*right*). (B) Fingerprint patterns averaged over the entire image for the images taken with a pixel dwell of 25 μs with the cooled (*top*) and uncooled (*bottom*) detector and (C) the corresponding shift vectors for the pixel reassignment in ISM. Some data points are not labeled for visualization purposes. (D) FRC-based resolution as a function of the pixel dwell time calculated from two independent images of the cell sample under the same experimental conditions. The continuous lines are single-exponential fits. The same FRC resolution of 326 nm can be obtained with a pixel dwell time of 25 μs and the detector at RT and with a pixel dwell time of 8.5 μs with a cooled detector (*dotted line*).

(Fig. 5). In spot-variation FFS, the autocorrelation curves are analyzed as a function of the focal (or detection) volume size to extract information about the (bio) molecular dynamics. In conventional spot-variation FCS, the detection volume can be adjusted by changing the radius of the confocal pinhole. In our SPAD-array-based implementation, we can obtain three different volumes in a single experiment by summing—in post-processing—the signals of multiple elements of the array, i.e., $I_{12}(t)$, $I_{sum3 \times 3}(t)$, and $I_{sum5 \times 5}(t)$) intensity time traces (15,16). To obtain the absolute sizes of the different detection volumes, which are needed to reveal the diffusion modality, one can use a reference sample with freely diffusing particles with a well-known diffusion coefficient. From the diffusion time, it is then possible to derive the volume size, typically the lateral $1/e^2$ radius ω of a detection volume approximated by a three-dimensional Gaussian. A different and more straightforward approach is scanning FCS with a fast (circularly) scanning laser beam on the sample of interest. In this work, we used the second approach. We per-

formed scanning FCS on a solution of fluorescent beads (20 nm in diameter) diluted in water, and we calculated the autocorrelation curves for the tree different detection volumes and for two different temperatures (Fig. 5 A), respectively, -15°C (cooled) and 25°C (uncooled, or RT). By fitting the correlation curves, we simultaneously extract the transit times and the detection volume sizes (Supporting materials and methods, Note S1). For the measurements at RT (Fig. 5 A, bottom), the amplitudes of the correlation curves differ approximately by a factor of 10 for the central pixel and 20 for Sum 3 × 3 and Sum 5 × 5— compared with the measurements with the cooled detector (Fig. 5 A, top). Because the amplitude is inversely proportional to the number of particles in the detection volume, this discrepancy leads to inconclusive results regarding the sample concentration when the detector is employed at RT. Moreover, at RT, the correlation curves go down at short lag times, below $\sim$100 μs, for bigger focal volumes (Sum 3 × 3 and Sum 5 × 5). This decrease, due to spurious negative correlations
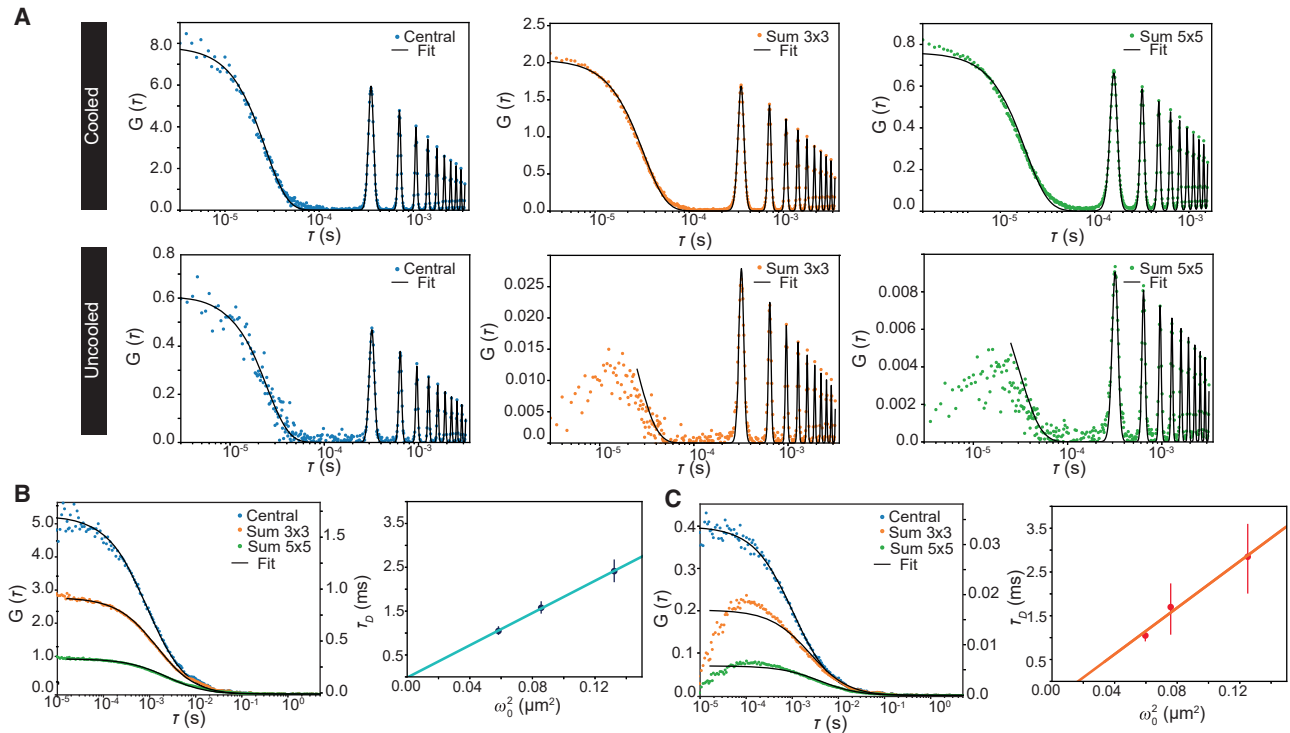

FIGURE 5 FFS measurements on fluorescent beads with a cooled (-15°C) vs. RT (25°C) SPAD array detector. Shown is a sample of freely diffusing fluorescent beads (diameter 20 nm). (A) Autocorrelation functions for a circular scanning measurement for the central pixel (left), Sum 3 × 3 (middle), and Sum 5 × 5 (right), for cooled (-15°C) and RT (25°C) detector. (B) Autocorrelation functions (left) for a single-point measurement for the central pixel, Sum 3 × 3, and Sum 5 × 5 with the cooled detector (-15°C). Note that the scale for Sum 3 × 3 and Sum 5 × 5 autocorrelation amplitudes are reported on the right y axis for visualization purposes. Given are diffusion times as a function of the focal volumes (right). The corresponding diffusion coefficients are (14 ± 1) μm^2/s for the central pixel, (14 ± 2) μm^2/s for Sum 3 × 3, and (14 ± 2)μm^2/s for Sum 5 × 5 (averages and standard deviations over five measurements of 200 s each). (C) Autocorrelation functions (left) for a single-point measurement for the central pixel, Sum 3 × 3, and Sum 5 × 5 with the RT (25°C) detector. Note that the scale for Sum 3 × 3 and Sum 5 × 5 autocorrelation amplitudes are reported on the right y axis for visualization purposes. Diffusion time as a function of the focal volume (right). The corresponding diffusion coefficients are (15 ± 2) μm^2/s for the central pixel, (12 ± 3) μm^2/s for Sum 3 × 3, and (12 ± 3) μm^2/s for Sum 5 × 5 (averages and standard deviations over five measurements of 200 s each).

at short timescales in some of the pixels, is also visible in the correlation functions for single-point acquisition FCS measurements with the uncooled detector (Fig. 5 C, *left*; (16)). We speculate that the decrease in the correlation is strictly connected with the dark noise signal. Indeed, 1) the correlation artifact vanishes when cooling the detector to −15°C (Fig. 5 B, *left*; Fig. S2); and 2), the artifact is more evident for relatively low fluorescence intensities, i.e., low SNRs. For example, in the single-point FCS experiment, the farther the SPAD array element from the center is, the lower the fluorescence signal is and the more negative the autocorrelation becomes (Fig. S2).

For the uncooled detector, the lack of accurate correlation values for short lag times precludes especially the study of fast diffusion processes: the correlation curves cannot simply be cropped, as is typically done to remove the after-pulsing effects. The artifacts in the autocorrelation curves at RT also affect the fitted diffusion times, i.e., the characteristic lag time where the autocorrelation reaches half of its amplitude and thus the observed diffusion modality. By using the sizes of the detection volumes extracted from the scanning FCS experiment (−15°C), we plotted the diffusion law for the single-point experiments at −15°C and at RT (Fig. 5 B, *right*; Fig. 5 C, *right*) At −15°C, the measured diffusion time scales, as expected, proportionally with the size of the detection volume (i.e., the beam waist), passing through the origin (Fig. 5 B, *right*), indicating that the beads are freely diffusing (36). The corresponding diffusion coefficient is (14 ± 1) μm^2/s, which is equivalent to a diameter of (27 ± 3) nm of the beads in accordance with the value provided by the manufacturer (actual size: 27 nm). On the other hand, without cooling (Fig. 5 C, *right*), the intercept of the linear fit with the y axis is negative, possibly linked with the artifacts caused by the high DCR present at RT. Notably, for the cooled detector, the autocorrelation curves do not show strong after-pulsing effects, not even at a relatively short lag time (500 ns, which is the minimal sampling time of the BrigthEyes-CDAQM (Fig. S2). This result confirms the excellent performance of the BCD SPAD array detector in terms of after-pulsing probability—also at −15°C. Moreover, we performed FCS experiments on highly concentrated fluorescent beads solutions to demonstrate the high dynamic range of the BCD SPAD array detector. Indeed, even with a count rate up to about 30 MHz, the FCS analysis is reliable: the diffusion times are constant over a wide range of count rates and the autocorrelation amplitude decreases as expected with increasing count rate (see Fig. S4).

To show the applicability of the cooled SPAD array detector, we performed FFS measurements in living cells. In particular, we performed FFS measurements in two different cell types, acquired with the cooled (−15°C) SPAD array detector (Fig. 6). First, we measured freely diffusing GFP in HEK293T cells (Fig. 6 A). To measure the type of diffusion of the fluorescent species expressed in the cells, we employed spot-variation FCS. The fluorescence fluctuations, acquired from the chosen position (represented by a *white circle* in Fig. 6) within the cell cytoplasm, are summed in a postprocessing stage to create the time traces $I_{12}(t)$, $I_{Sum3 \times 3}(t)$, and $I_{Sum5 \times 5}(t)$) for the different detection volumes. Here, the autocorrelation functions for the three focal volumes (Fig. 6 A, *middle*) central, *Sum* 3×3, and *Sum* 5×5) are analyzed with a single freely diffusing component FCS model. Indeed, the diffusion law confirms, as expected, a freely diffusing fluorescent species (Fig. 6 A, *right*), where the diffusion times scale proportionally with the focal area. Secondly, we investigated a more complex cell system. In particular, we registered the fluorescent fluctuations at different positions—within the cell cytoplasm (Fig. 6 B) and the nucleus (Fig. 6 C)—of U2-OS cells expressing eGFP-DEK fusion protein, a chromatin architectural protein (37). In the cell cytoplasm, DEK-GFP proteins are diffusing freely. Indeed, the spot-variation analysis (Fig. 6 C) reveals the free diffusion of these proteins, as the measured diffusion times scale proportionally with the focal volume. By fitting the autocorrelation curves with a single freely diffusing component FCS model, we found a diffusion coefficient of (38 ± 14) μm^2/s (Fig. 6 B). However, when we acquired the FFS measurements in the nuclei of these cells (Fig. 6 C), eGFP-DEK is not freely diffusing anymore. The single freely diffusing component FCS model fails to fit the autocorrelation curves acquired in the nuclei, and instead, an anomalous diffusion model has to be employed (Fig. 6 C, *middle*). In this case, the diffusion time versus beam waist curve does not pass through the origin, but the intercept is greater than 0, confirming the anomalous mobility of eGFP-DEK in the cell nuclei.

CONCLUSIONS

FLSM typically uses single-element detectors. Thanks to the continuous progress made on well-established technologies, such as PMTs and SPADs, and the introduction of new technologies, such as HyDs and SiPMs, the performance of FLSM constantly improved and new applications emerged. However, since the 1980s, it was known that FLSM imaging would benefit from a detector able to also record the spatial distribution of the fluorescence signal for each scan position (i.e., pixel) instead of integrating such a distribution across the sensitive area, as for single-element detectors. More recently, it has been demonstrated that having access to this spatial information is also important for FFS.
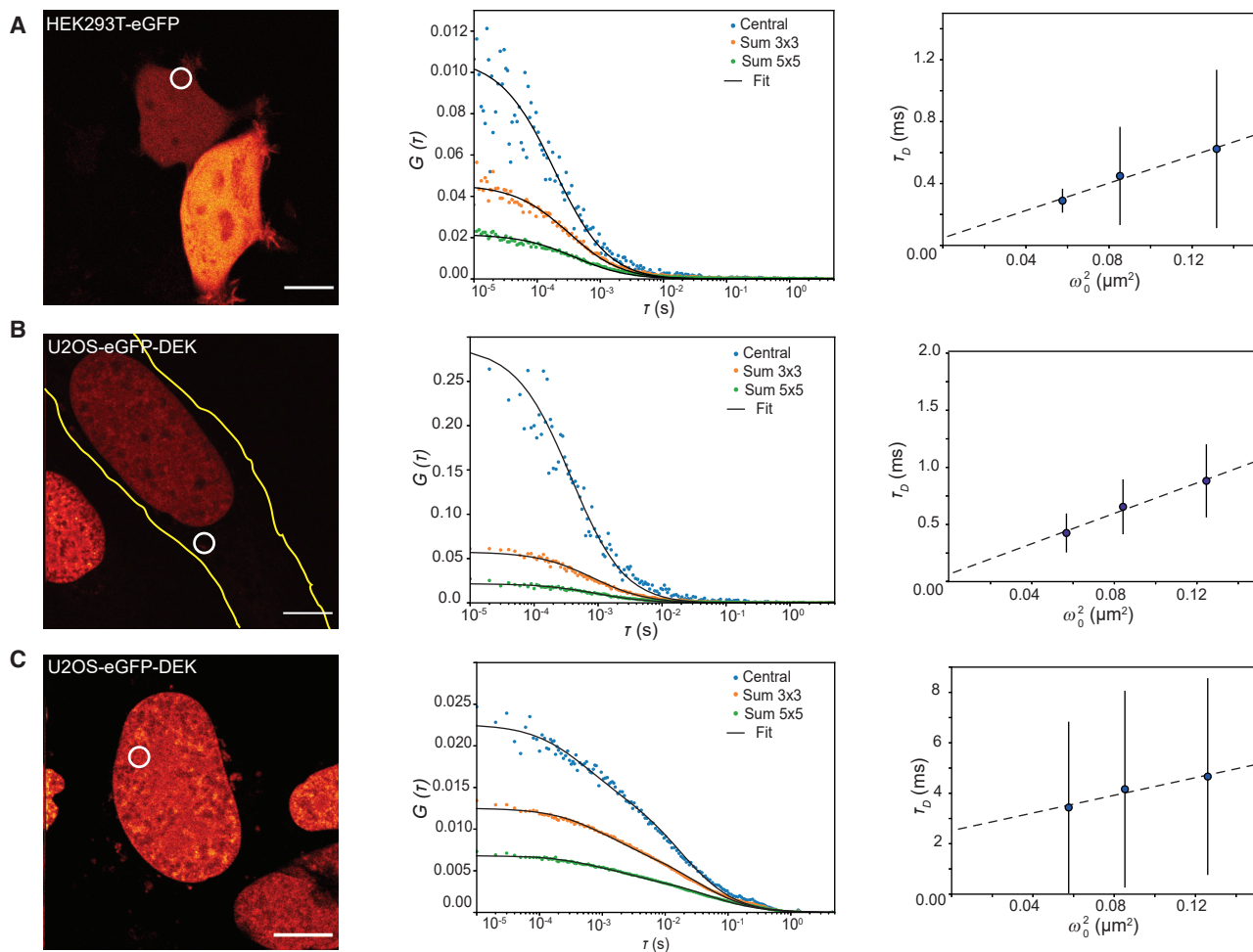
FIGURE 6 FFS measurements on live cells expressing eGFP or a GFP-tagged protein with the cooled detector. Shown is a sample of U2-OS cells expressing DEK-eGFP and HEK293T cells expressing GPF only. (*A*) ISM image (*left*) of an HEK293T-cell-expressing eGFP, autocorrelation curves (*middle*) for the central pixel, *Sum* 3×3, and *Sum* 5×5 acquired in the marked position in the cytoplasm of the cell with the cooled ($-15°$C) detector and diffusion time as a function of the focal volume (*right*). Average and standard deviations over five cells in 10 different positions within the cell cytoplasm. (*B*) ISM image (*left*) of a U2-OS cell expressing eGFP-DEK fusion protein (the *yellow line* marks approximately the cell outline), autocorrelation curves (*middle*) for the central pixel, *Sum* 3×3, and *Sum* 5×5 acquired in the marked position in the cytoplasm of the cell with the cooled ($-15°$C) detector and diffusion time as a function of the focal volume (*right*). Average and standard deviations over eight cells in 18 different positions within the cytoplasm. (*C*) ISM image (*left*) of a U2-OS cell expressing eGFP-DEK, autocorrelation curves (*middle*) for the central pixel, *Sum* 3×3, and *Sum* 5×5 acquired in the marked position in the nucleus of the cell with the cooled ($-15°$C) detector and diffusion time as a function of the focal volume (*right*). Average and standard deviations over five cells in eight different positions within the cell nuclei. The white circles mark where the FFS measurements were acquired. The scale bars represent 10 μm.

SPAD array detectors are currently the best candidate to provide this spatial information and thus to overcome this limitation of FLSM while maintaining the excellent characteristics of state-of-the art single-element detectors.

In this work, we proposed a new—to our knowledge—cooled SPAD array detector, and we showed how cooling the SPAD array is beneficial for imaging and can even be necessary for FFS. For imaging, cooling the detector decreases the DCR, which leads to a better SNR and consequently a higher contrast and better resolution. In comparison with the uncooled detector, images can be taken at almost three times the speed or a three times lower laser power for the same image quality. This is especially important for long-term live-cell imaging in which the laser powers have to be kept low to reduce phototoxicity effects and photobleaching during time-lapse experiments, and the pixel dwell time sets the frame-rate of the temporal series. This last aspect is particularly important for the combination resonant scanner and SPAD array detector: the number of line-scans to achieve a significant SNR can be reduced. For FFS, cooling the detector is necessary to remove artifacts in the correlation curves at short lag times and to get reliable results for the concentration and the diffusion time.

An underestimated characteristic of SPAD array detectors is their absence of read-out noise. Reducing the DCR of such a detector therefore effectively allows imaging affected by photon-counting noise only. Notably, single-photon megapixel CMOS cameras have also been proposed in the context of wide-field imaging. We expect that having access to truly photon-counting imaging will open up new exciting data analysis and reconstruction methods.

Despite the improvements shown in this study, the usage of SPAD array technology in the context of FLSM is a very recent development. The majority of these SPAD array detectors has been extensively optimized for other applications, such as light detection and ranging. Consequently, there is still room for FLSM optimization. In this scenario, it is important to highlight that the fabrication cost is not a major issue. For example, the DCR can be further improved by reducing the area of each SPAD element, which however comes with a fill-factor decrease. Microlenses can solve this problem by increasing the effective fill factor while maintaining the small size of the individual SPAD elements. The PDE in the far-red region is another important issue as this wavelength range has a higher penetration depth and is very suitable for live-cell imaging. Although BCD technology represents an important improvement with respect to CMOS, the PDE in this range is still inferior to the so-called thick SPAD (approaching 70% at 633 nm). A reduction of the afterpulsing probability is also important for having a high dynamic range. Indeed, a low after-pulsing probability allows for a short hold-off. With our BCD SPAD array, we show FFS measurements at >30 MHz count rate thanks to the low after-pulsing probability, even at 25 ns hold-off. However, reaching the few-nanosecond dead time of a HyD would further improve the dynamic range. Finally, a larger number of SPAD elements, while keeping the asynchronous read-out scheme (e.g., 7 × 7), would be beneficial for all applications and may trigger new ones. For FFS, the signal from a larger number of detection volumes can be collected simultaneously. For imaging, a method for estimating the out-of-focus light can be implemented. We also anticipate the benefit of having a larger SPAD array detector for combining single-molecule techniques with FLSM.

In summary, the reduction of dark noise obtained by cooling the detector, the enhancement of quantum efficiency by means of new SPAD fabrication technologies (e.g., the BCD), and in perspective, the increased effective fill factor with microlenses, the major versatility with larger SPAD arrays (e.g., 7 × 7), and the combination with single-molecule techniques are substantially reducing the motivations to not install a SPAD array detector in any FLSM.

AUTHOR CONTRIBUTIONS

M.B., G.T., F.V., A.T., and G.V. conceived the idea. M.B., E.C., F.V., and A.T. developed the cooling system for the detector. E.S., E.P., G.T., and G.V. designed and realized the optical setup. E.S., G.T., and G.V. designed and implemented the BrightEyes-CDAQM starting from Carma Technology. E.S. and E.P. developed the software analysis for the FFS experiments. E.S., G.T., and G.V. developed the software for image reconstruction. E.S., E.P., M.B., G.T., F.V., E.M.P., A.B., A.T., and G.V. designed the experiments. E.S., E.P., M.B., G.T., and E.C. characterized the SPAD array detector. E.S., E.P., and S.Z. performed the FFS and imaging experiments and analyzed the data with G.V. S.Z., A.P.-M., and E.M.P. prepared the fixed and live cells. E.P., A.P.-M., S.Z., and E.M.P. analyzed the live-cell experiments. E.S., F.V., A.B., A.T., and G.V. supervised the project. E.S., E.P., and G.V. wrote the article with contributions from all of the authors.

DECLARATION OF INTERESTS

G.V. has personal financial interest (co-founder) in Genoa Instruments.

REFERENCES

1. Martinez-Moro, M., D. Di Silvio, and S. E. Moya. 2019. Fluorescence correlation spectroscopy as a tool for the study of the intracellular dynamics and biological fate of protein corona. *Biophys. Chem.* 253:106218.

2. Macháň, R., and T. Wohland. 2014. Recent applications of fluorescence correlation spectroscopy in live systems. *FEBS Lett.* 588:3571–3584.

3. Yu, L., Y. Lei, …, P. Gao. 2021. A comprehensive review of fluorescence correlation spectroscopy. *Front. Phys.* 9:644450.

4. Donati, S., and T. Tambosso. 2014. Single-photon detectors: from traditional PMT to solid-state SPAD-based technology. *IEEE J. Sel. Top. Quantum Electron.* 20:204–211.

5. Bronzi, D., F. Villa, …, F. Zappa. 2016. SPAD figures of merit for photon-counting, photon-timing, and imaging applications: a review. *IEEE Sens. J.* 16:3–12.

6. Acerbi, F., A. Ferri, …, C. Piemonte. 2014. Characterization of single-photon time resolution: from single SPAD to silicon photomultiplier. *IEEE Trans. Nucl. Sci.* 61:2678–2686.

7. Schneider, F., P. Hernandez-Varas, …, I. Urbančič. 2020. High photon count rates improve the quality of super-resolution fluorescence fluctuation spectroscopy. *J. Phys. D: Appl. Phys.* 53:164003.

8. Buzhan, P., D. Dolgoshein, …, S. Smirnov. 2003. Silicon photomultiplier and its possible applications. *Opt. Lett.* 504:48–52.

9. Schweikhard, V., L. A. J. Alvarez, …, A. Giske. 2020. Application note: the power HyD family of detectors. *Nat. Methods.* 17.

10. Bertero, M., C. D. Mol, …, J. G. Walker. 1984. Resolution in diffraction-limited imaging, a singular value analysis. IV. The case of uncertain localizaiton or non uniform illumination object. *Opt. Acta (Lond.).* 31:923–946.

11. Sheppard, C. J. 1988. Super-resolution in confocal imaging. *Optik (Stuttg.).* 80:53–54.

12. Müller, C. B., and J. Enderlein. 2010. Image scanning microscopy. *Phys. Rev. Lett.* 104:198101.

13. Huff, J. 2015. The airyscan detector from Zeiss: confocal imaging with improved signal-to-noise ratio and super-resolution. *Nat. Methods.* 12:1–2.

14. Castello, M., G. Tortarolo, …, G. Vicidomini. 2019. A robust and versatile platform for image scanning microscopy enabling super-resolution FLIM. *Nat. Methods.* 16:175–178.

15. Scipioni, L., L. Lanzanó, …, E. Gratton. 2018. Comprehensive correlation analysis for super-resolution dynamic fingerprinting of cellular compartments using the Zeiss Airyscan detector. *Nat. Commun.* 9:5120.

16. Slenders, E., M. Castello, …, G. Vicidomini. 2021. Confocal-based fluorescence fluctuation spectroscopy with a SPAD array detector. *Light Sci. Appl.* 10:31.

17. Sroda, A., A. Makowski, …, R. Lapkiewich. 2020. SOFISM: super-resolution optical fluctuation image scanning microscopy. *Optica.* 7:1308–1316.

18. Tenne, R., U. Rossman, …, D. Oron. 2019. Super-resolution enhancement by quantum image scanning microscopy. *Nat. Photonics.* 13:116–122.

19. Scarcella, C., A. Tosi, …, F. Zappa. 2013. Low-noise low-jitter 32-pixels CMOS single-photon avalanche diodes array for single-photon counting from 300 nm to 900 nm. *Rev. Sci. Instrum.* 84:123112.

20. Bruschini, C., H. Homulle, …, E. Charbon. 2019. Single-photon avalanche diode imagers in biophotonics: review and outlook. *Light Sci. Appl.* 8:87.

21. Sanzaro, M., P. Gattari, …, F. Zappa. 2018. Single-photon avalanche diodes in a 0.16 μm BCD technology with sharp timing response and red-enhanced sensitivity. *IEEE J. Sel. Top. Quantum Electron.* 24:1–9.

22. Buttafava, M., F. Villa, …, A. Tosi. 2020. SPAD-based asynchronous-readout array detectors for image-scanning microscopy. *Optica.* 7:755–765.

23. Grove, A. S. 1967. Physics and Technology of Semiconductor Devices. John Wiley & Sons, Inc., New York, p. 392.

24. Castello, M. 2017. Carma: a novel super-resolution microscopy platform. University of Genoa, PhD thesis.

25. Castello, M., G. Tortarolo, …, G. Vicidomini. 2017. Removal of anti-Stokes emission background in STED microscopy by FPGA-based synchronous detection. *Rev. Sci. Instrum.* 88:053701.

26. Sankaranarayanan, S., D. De Angelis, …, T. A. Ryan. 2000. The use of pHluorins for optical measurements of presynaptic activity. *Biophys. J.* 79:2199–2208.

27. Petrini, E. M., T. Ravasenga, …, A. Barberis. 2014. Synaptic recruitment of gephyrin regulates surface GABAA receptor dynamics for the expression of inhibitory LTP. *Nat. Commun.* 5:3921.

28. Petrini, E. M., T. Nieus, …, A. Barberis. 2011. Influence of GABAAR monoliganded states on GABAergic responses. *J. Neurosci.* 31:1752–1761.

29. Koho, S., G. Tortarolo, …, G. Vicidomini. 2019. Fourier ring correlation simplifies image restoration in fluorescence microscopy. *Nat. Commun.* 10:3103.

30. Koho, S. V., E. Slenders, …, G. Vicidomini. 2020. Two-photon image-scanning microscopy with SPAD array and blind image reconstruction. *Biomed. Opt. Express.* 11:2905–2924.

31. Tortarolo, G., M. Castello, …, G. Vicidomini. 2018. Evaluating image resolution in stimulated emission depletion microscopy. *Optica.* 5:32–35.

32. Müller, P. 2012. Python multiple-tau algorithm. Python, version 0.3.3 https://pypi.org/project/multipletau/.

33. Petrásek, Z., and P. Schwille. 2008. Precise measurement of diffusion coefficients using scanning fluorescence correlation spectroscopy. *Biophys. J.* 94:1437–1448.

34. Anti, M., A. Tosi, …, F. Zappa. 2011. Modeling of afterpulsing in single-photon avalanche diodes. *In* Physics and Simulation of Optoelectronic Devices XIX B. Witzigmann, F. Henneberger, Y. Arakawa, and A. Freundlich, eds.. SPIE.

35. Ishii, K., and T. Tahara. 2015. Correction of the afterpulsing effect in fluorescence correlation spectroscopy using time symmetry analysis. *Opt. Express.* 23:32387–32400.

36. Wawrezinieck, L., H. Rigneault, …, P. F. Lenne. 2005. Fluorescence correlation spectroscopy diffusion laws to probe the submicron cell membrane organization. *Biophys. J.* 89:4029–4042.

37. Waldmann, T., I. Scholten, …, R. Knippers. 2004. The DEK protein—an abundant and ubiquitous constituent of mammalian chromatin. *Gene.* 343:1–9.